Article

A Synchronous Tuning Control System for Very Low Frequency Communication Based on Real-Time Impedance Detection

Shize Wei, Xu Xie *, Yuqing Liu and Hao Zuo

College of Electronics Engineering, Naval University of Engineering, Wuhan 430030, China;
fanxrcwsz15@alumni.nudt.edu.cn (S.W.); liuyuqing6044@163.com (Y.L.); youdangxiaowoniu@163.com (H.Z.)
* Correspondence: 1109031069@nue.edu.cn; Tel.: +86-186-2709-8922

Abstract: A Very Low Frequency (VLF) communication system is a communication system with limited transmit bandwidth, mainly because the VLF antenna is a high-Q electrically small antenna (ESA) with a narrow effective bandwidth, which limits the improvement of communication rate. To achieve broadband VLF communication, the commonly used method is synchronous tuning technology. In this paper, a synchronous control algorithm based on real-time impedance detection and a synchronous control system structure are proposed. Simulation results show that the method can improve the antenna matching performance, increase the effective bandwidth of the antenna feeder system, and improve the signaling rate.

Keywords: VLF communication; ESA; impedance detection; synchronous tuning techniques; logic gate

1. Introduction

A VLF antenna is a typical electrically small antenna [1,2], the electrically small antenna (ESA) is the antenna whose antenna size is much smaller than the wavelength ($l \ll \lambda$), which can be equivalent to a capacitor or inductor with a small radiation resistance, which also leads to the ESA having a high quality factor, Q. Q is inversely proportional to the antenna bandwidth, so the electrically small antenna with high Q is a narrow band antenna. Chu's theorem gives the formula for calculating the Q value of electrically small antennas as follows [1–3].

$$Q = \frac{1 + 3k^2a^2}{(ka)^3(1 + k^2a^2)} \tag{1}$$

k is the wave number, $k = 2\pi/\lambda$, and as shown in Figure 1, a is the radius of the sphere that exactly surrounds the antenna. It can be known from Equation (1) that when the antenna electrical size decreases, the Q value will increase and the antenna bandwidth will become narrow. When the antenna size decreases to less than $\lambda/2\pi$, the Q value will increase greatly.
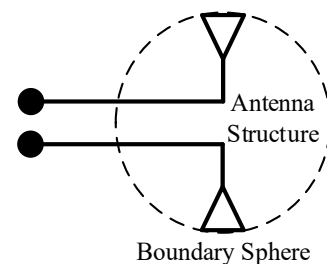
Figure 1. Schematic diagram of the ESA.

At present, the VLF communication system mainly uses an MSK (Minimum Shift Keying) signal source [4,5], and the traditional VLF transmitter system uses a fixed tuning network, and the resonant frequency of the antenna feeder system is at the center

frequency of the MSK signal. In order to ensure that the transmitted signal has enough power, the symbol rate of the MSK signal will be very low, which also leads to a low communication rate.

$$S_{MSK} = cos(2\pi f_c t + \frac{\pi a_k}{2T_s}t + \varphi_k), (k-1)T_s \leq t \leq kT_s \tag{2}$$

Formula (2) is the expression of MSK signal [6], where f_c is the carrier frequency; $a_k = \pm 1$ (corresponding to the input symbol is "1" or "0"); T_s is the symbol width; φ_k is the initial phase of the kth symbol, which is invariant in one symbol width. When the input symbol is "1", $a_k = +1$, frequency is $f_h = f_c + 1/4T_s$, and when the input symbol is "0", $a_k = -1$, frequency is $f_l = f_c - 1/4T_s$ and symbol rate is $R_B = 1/T_s$. In this paper, f_h is the "mark" frequency and f_l is the "space" frequency.

According to the Shannon formula $C = B \log_2(1 + S/N)$ [6], under the condition that SNR is almost unchanged, as the communication rate increases, the communication capacity increases, and the bandwidth occupied by the signal also gradually increases. However, when the signal bandwidth exceeds the available bandwidth of the antenna feeder system, the signal will be greatly attenuated and the information carried by the waveform will be lost.

Therefore, the reason that limits the improvement of the communication rate lies in the narrowband characteristics of the high-Q electric small antenna. In order to enhance the effective bandwidth and optimize the communication rate of the VLF system, two primary approaches can be employed. One involves augmenting the series resistance between the antenna and transmitter; however, this comes at a cost of reduced efficiency, which may impact the overall communicative capability of the system [7].

Another approach to enhance the effective bandwidth is synchronous tuning technology [8], enabling the feeder system to dynamically tune to both the "space" frequency f_l and "transmission" frequency f_h of MSK signals instead of being statically tuned at the center frequency. This technique effectively broadens the system's effective bandwidth and enhances communication speed without compromising antenna efficiency, as depicted in Figure 2 [9–14]. Presently, countries such as the United States and Australia have embraced synchronous tuning technology, achieving communication speeds ranging from 200 bps to 1000 bps or even higher [15].
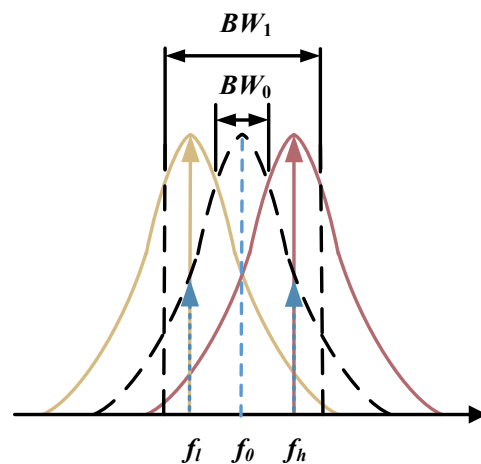
Figure 2. Schematic of the effective bandwidth of a high-Q ESA (The black curve represents the antenna bandwidth, while the yellow and red curves represent the bandwidth occupied by the MSK signal).

This technology has been developing continuously for many years and has achieved good results, including magnetic saturation switching amplifier methods, frequency shift keying methods based on electronic switching capacitors, high current variable inductor methods and so on [16–21]. Based on the above methods, A synchronous tuning control

strategy for VLF communication based on real-time impedance detection is proposed in this paper. The resonant frequency of antenna feeder system is controlled by symbol signal and impedance detection result. This method can quickly determine the inductance of antenna feeder system and then control the corresponding inductor in the controlled inductor array.

2. Basic Structure of the System

As shown in Figure 3, C_a is the equivalent capacitor of the VLF antenna, R_a is the equivalent radiation resistor of the VLF antenna, L_0 is the fixed tuning inductor, and ΔL is the variable inductor, which is specifically composed of different combinations of controlled inductor arrays (L_{cn}) in this paper. When the frequency of the MSK signal is f_h, the tuning inductance required for this system is L_0 and $\Delta L = 0$. When the frequency of the MSK signal is f_l, the required tuning inductance for this system becomes $L_0 + \Delta L$, $\Delta L = 1/(\omega_l^2 C_a) - L_0$.
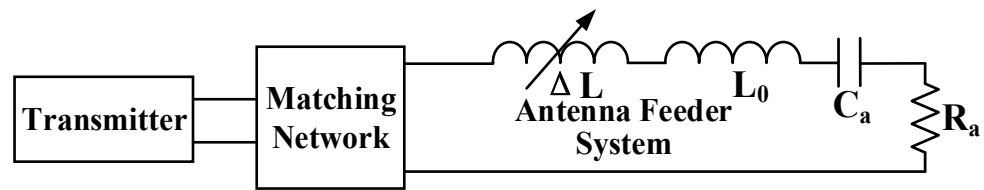

Figure 3. Equivalent circuit diagram of VLF signaling system (ignoring loss resistance) [17].

Figure 4 shows the structure diagram of the synchronous Tuning Control described in this paper. The system is mainly composed of the controlled inductance matrix, the driver and switch matrix, and the control matrix. L_0 is the fixed inductor and L_{C1} and L_{C2} are the controlled inductors, which form the primary loop through the MSK signal, and when the MSK signal carrier frequency is f_h, all IGBTs are in the conduction state [22,23]. At this time, only the inductor L_0 is in operation in the system. Then, the resonant frequency of the antenna feeder system is adjusted to f_h when the MSK signal carrier frequency is f_l. The IGBT of the corresponding numerical inductor Lcn is controlled to be turned off, so that the inductance in the antenna feeder system is $L_0 + \sum_{i=1}^{n} L_{cn}, n \in N+$, and the resonant frequency of the antenna feeder system is adjusted to f_l.
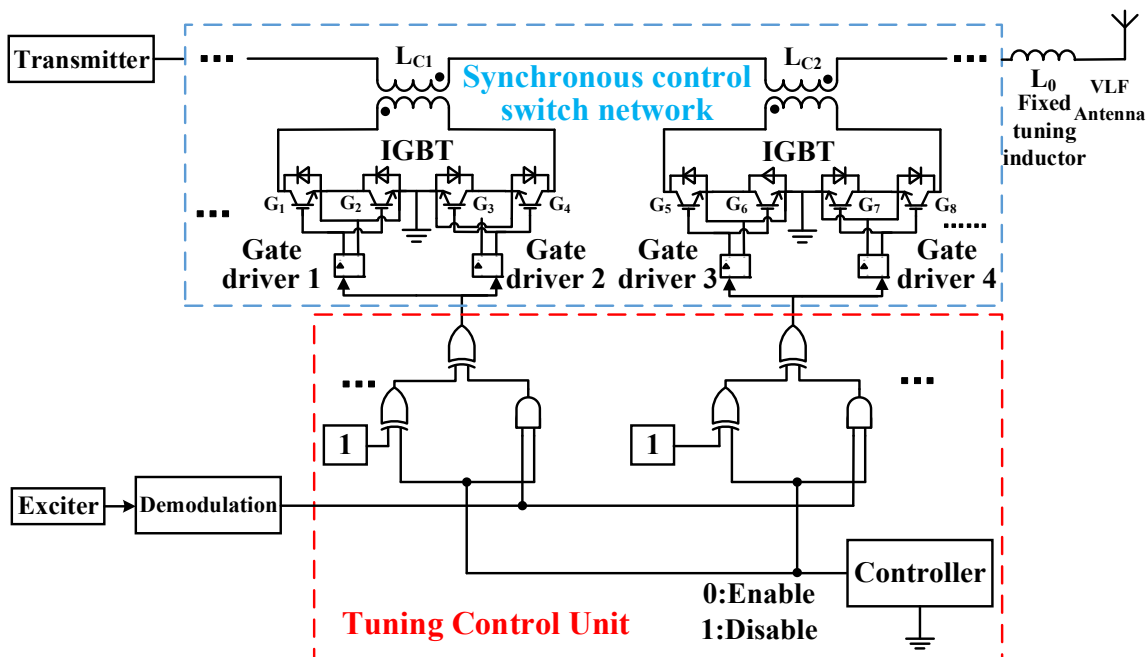

Figure 4. Schematic diagram of the synchronous control system described.

As shown in Figure 4, the key part of the system is the control matrix, and the controller is used to control the enable state of each logic unit. Now, the function of the logic control unit is mainly expounded. As shown in Figure 5, each output port of the controller corresponds to one logic control unit, and each logic control unit is composed of two XOR gates and one AND gate. The AND gate input is the control signal output from the controller port and the demodulated MSK symbol signal, the XOR gate input to the left of the AND gate is logic 1 and the control signal output from the controller port, and the XOR gate input above is the AND gate and the logic output of the XOR gate to the left of the AND gate. The logic truth table is as follows [24]:
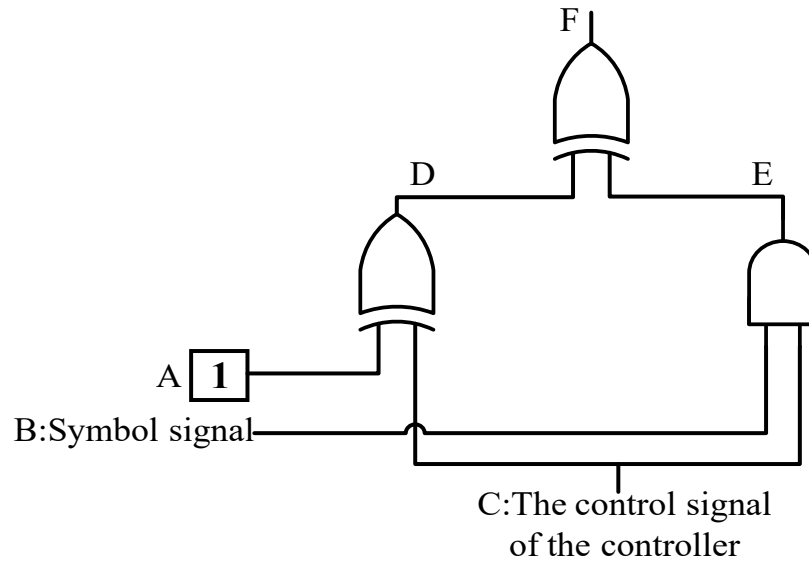
Figure 5. Logic control unit diagram (A is a fixed logic instruction, D and E are the outputs of XOR and AND gates, respectively, and F is the final control instruction output by the logic control unit.).

As can be seen from Table 1, when the controller outputs logic 0, the logic output of F is always 1, which is not affected by the symbol signal. At this time, the IGBT always remains in the conduct state, and the logic 0 output by the controller is called the failure instruction.

Table 1. Logic truth table.

A	B: Symbol Signal	C: Controller Signal	D	E	F
1	1	0	1	0	1
1	0	0	1	0	1
1	1	1	0	1	1
1	0	1	0	0	0

When the controller outputs logic 1, the logic output of F is controlled by the symbol signal. When the symbol is 1, F is 1, and when the symbol is 0, F is 0. At this time, the IGBT is in the symbol signal control state, and the logic 1 output by the controller is called the enabling instruction.

After ΔL is calculated, the corresponding controller port is determined by the table look-up method, and the corresponding port will always remain in the enabled state.

3. Synchronous Control Strategy Based on Real-Time Impedance Detection

Basic condition: The high level of the control signal corresponds to the high frequency point f_h of the MSK signal, and the low level corresponds to the low frequency point, f_l, of the MSK signal. The system is resonant at high frequency by adjusting the fixed

tuning inductor, L_0, and the initial state of the power electronic switches at both ends of the controlled inductor is conduction.

Figure 6 shows the flow of synchronous control strategy based on real-time impedance detection (hereinafter referred to as SYNT-RTID synchronous control strategy). The calculation process of the controlled inductance, ΔL, is as follows [16].

$$Z = \frac{\dot{U}}{\dot{I}} = \frac{U\angle\varphi_u}{I\angle\varphi_i} = |Z|\angle\varphi_Z = z\angle\varphi_Z \tag{3}$$

$$Z = \frac{\dot{U}}{\dot{I}} = R + j(\omega L - \frac{1}{\omega C}) \tag{4}$$

$$\omega L - \frac{1}{\omega C} = z\sin\varphi_Z \tag{5}$$

$$L = \frac{z\sin\varphi_Z}{\omega} + \frac{1}{\omega^2 C} \tag{6}$$

$$\Delta L = \frac{\text{Im}[Z]}{\omega} = \frac{z\sin\varphi_Z}{\omega} \tag{7}$$
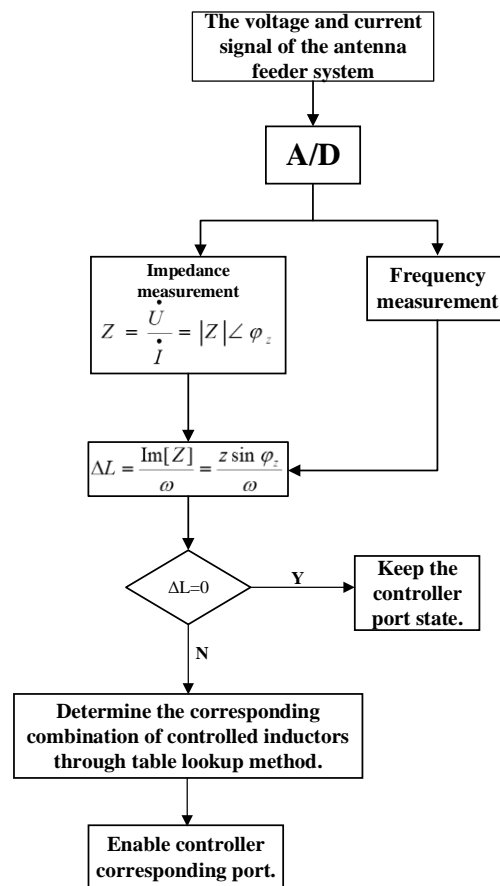

Figure 6. Flowchart of synchronous control strategy based on real-time impedance detection.

As shown in Figure 6, after ΔL is obtained, the appropriate combination of controlled inductors is selected by the table look-up method. Each ΔL corresponds to a group of controlled inductor combinations, and each controlled inductor corresponds to the control port of a controller to ensure that the controller can control the corresponding number of inductors.

The actual accuracy of the inductor is difficult to reach the accuracy of the theoretical value. At the same time, considering the cost, the accuracy of the inductor should also be controlled within a reasonable range. The VLF communication system is a narrowband system, and the accuracy of the inductor has a great impact on the system. We mainly discuss the influence of the inductor accuracy on the power factor angle, φ, and the antenna radiation efficiency of the antenna feeder system.

For the convenience of discussion, in this section, the antenna equivalent capacitance is $C_a = 39.79$ nF, the antenna equivalent radiation resistance is $R_a = 1\ \Omega$, the MSK signal center frequency, f_0, are 15 kHz, 20 kHz, 25 kHz, and 30 kHz, respectively, and the symbol rate, R_B, is 200 bps, 300 bps, 500 bps, 700 bps, and 900 bps. L_0 is the amount of tuning inductance required by the antenna fed system at frequency f_h resonant, and L_l is the amount of tuning inductance required by the antenna fed system at frequency f_l resonant, and $\Delta L = L_l - L_0$. The heat loss is ignored in this paper.
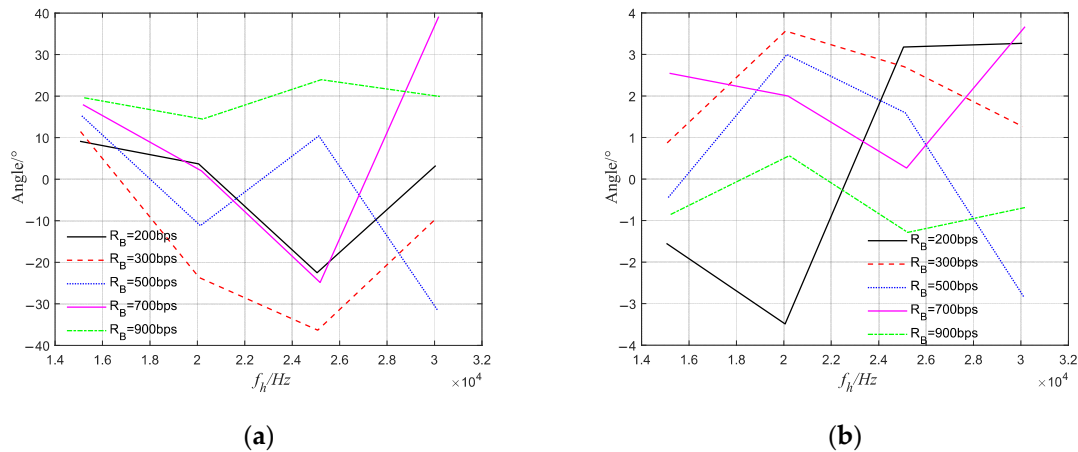
3.1. Power Factor Angle of Antenna Feeder System

The power factor cosφ is the ratio of active power, P, to apparent power, S, in an AC circuit, commonly represented as λ. φ is referred to as the power factor angle and can be obtained by subtracting the phase of port current from the phase of port voltage [25–27]. Let us assume:

$$\dot{U} = U\angle\varphi_u \tag{8}$$

$$\dot{I} = I\angle\varphi_i \tag{9}$$

$$\varphi = \varphi_u - \varphi_i \tag{10}$$

According to Equations (8)–(10), we can obtain the power factor angle, φ, of the antenna feeder system, as shown in Section 3.1 and Figure 8.

(**a**)   (**b**)

Figure 7. The power factor angle, φ, of the antenna feeder system when the carrier frequency of the MSK signal is f_h (**a**) The power factor angle, φ, of the antenna feeder system when the accuracy of L_0 reaches n $\times 10^{-2}$ mH; (**b**) The power factor angle, φ, of the antenna feeder system when the accuracy of L_0 reaches $n \times 10^{-3}$ mH.

According to Section 3.1 and Figure 8, when the accuracy of L_0 and L_l is n $\times 10^{-2}$ mH, the power factor angle, φ, of the antenna feeder system is approximately between $-40°$ and $+40°$, which translates to a power factor of approximately $0.766 < \cos\varphi < 1$. When the accuracy of L_0 and L_l is n $\times 10^{-3}$ mH, the power factor angle, φ, of the antenna feeder system is approximately between $-4°$ and $4°$, which translates to a power factor of approximately $0.998 < \cos\varphi < 1$. It can be seen that the improvement of accuracy greatly reduces the power factor angle PHI of the antenna feeder system, and we can consider that the voltage signal and the current signal are approximately in phase. In general, $\cos\varphi > 0.8$ is required [27].

(**a**) (**b**)
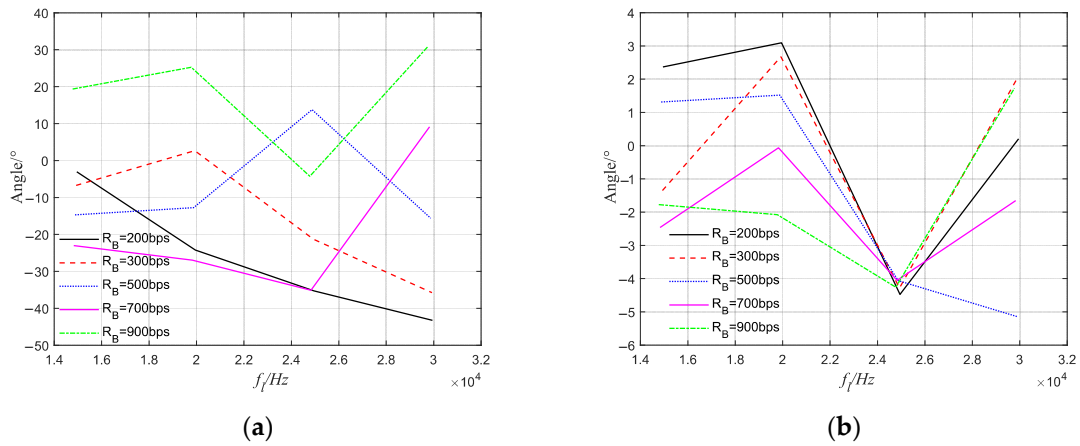
Figure 8. The power factor angle, φ, of the antenna feeder system when the carrier frequency of the MSK signal is f_l (**a**) The power factor angle, φ, of the antenna feeder system when the accuracy of L_0 reaches n $\times 10^{-2}$mH; (**b**) The power factor angle, φ, of the antenna feeder system when the accuracy of L_0 reaches $n \times 10^{-3}$mH.
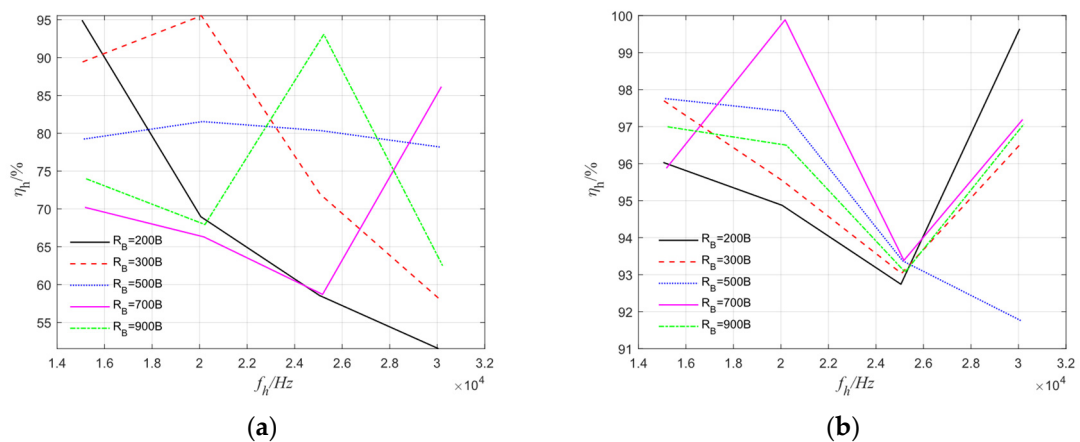
3.2. Radiation Efficiency of the Antenna

The apparent power, S, of the antenna feeder system includes the active power, P_a, and the reactive power, Q. In this paper, P_a is the antenna radiated power [4].

$$P_a = R_a \times \overset{\bullet 2}{I} \tag{11}$$

$$Q = \left| \omega L - \frac{1}{\omega C_a} \right| \times \overset{\bullet 2}{I} \tag{12}$$

$$\eta = \frac{P_a}{P_a + Q} = \frac{R_a}{R_a + \left| \omega L - \frac{1}{\omega C_a} \right|} \tag{13}$$

It can be seen from Figures 9 and 10 that when the accuracy of L_0 and L_l is n $\times 10^{-2}$mH (n is a positive integer, for example, n = 1, which means that the inductance is N), the variation range of antenna radiation efficiency is about 50% to 95%, and the variation range of antenna radiation efficiency is large and the decline is obvious. When the accuracy of L_0 and L_l is n $\times 10^{-3}$mH, the variation range of antenna radiation efficiency is about 91% to 100%.

(**a**) (**b**)

Figure 9. The antenna radiation efficiency when the carrier frequency of the MSK signal is f_h. (**a**) The antenna radiation efficiency when the accuracy of L_0 reaches n $\times 10^{-2}$mH; (**b**) the antenna radiation efficiency when the accuracy of L_0 reaches n $\times 10^{-3}$mH.

(**a**)　　　　　　　　　　　　　　　　　(**b**)
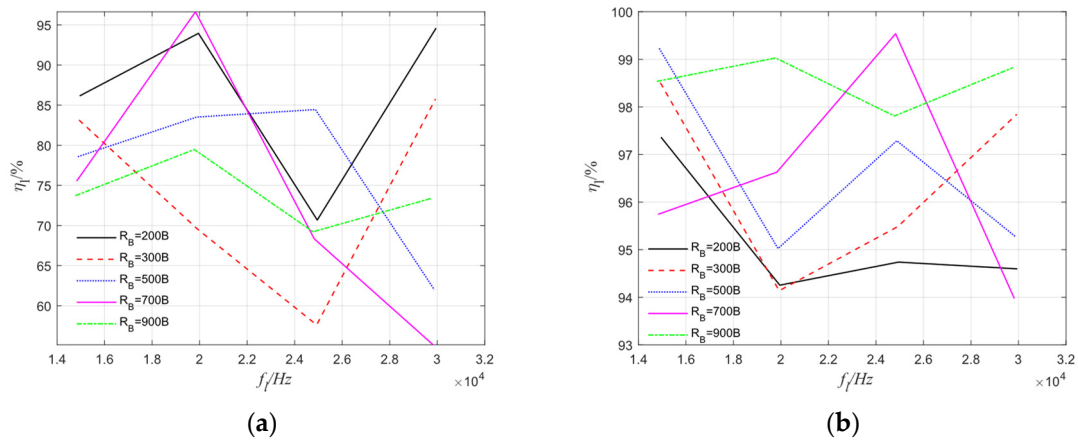
Figure 10. The antenna radiation efficiency when the carrier frequency of the MSK signal is f_l. (**a**) The antenna radiation efficiency when the accuracy of L_l reaches n $\times 10^{-2}$ mH; (**b**) the antenna radiation efficiency when the accuracy of L_l reaches n $\times 10^{-3}$ mH.

Considering that there are many factors that affect the performance of the communication system, the superposition of multiple factors may lead to a serious degradation of the system performance, so the influence of the accuracy of the inductor on the system performance should be as little as possible. Combining Sections 3.1 and 3.2 , the accuracy of L_0 and L_l is at least n $\times 10^{-3}$ mH under the proposed conditions in this paper, and at this time, we can obtain Tables 2 and 3.

Table 2. Inductance values L_0/mH corresponding to different Baud rates and center frequencies.

f_0 / L_0 / R_B	15 kHz	20 kHz	25 kHz	30 kHz
100 bps	2.820	1.588	1.017	0.706
200 bps	2.811	1.584	1.014	0.705
300 bps	2.801	1.580	1.012	0.704
400 bps	2.792	1.576	1.01	0.703
500 bps	2.783	1.572	1.008	0.701
600 bps	2.774	1.568	1.006	0.700
700 bps	2.764	1.564	1.004	0.699
800 bps	2.755	1.560	1.002	0.698
900 bps	2.746	1.556	1.000	0.697
1000 bps	2.737	1.552	0.998	0.696

Table 3. Inductance values L_l/mH corresponding to different Baud rates and center frequencies.

f_0 / L_l / R_B	15 kHz	20 kHz	25 kHz	30 kHz
100 bps	2.839	1.595	1.021	0.709
200 bps	2.848	1.599	1.023	0.710
300 bps	2.858	1.604	1.025	0.711
400 bps	2.867	1.608	1.027	0.712
500 bps	2.877	1.612	1.029	0.713

Table 3. *Cont.*

f_0 L_l R_B	15 kHz	20 kHz	25 kHz	30 kHz
600 bps	2.887	1.616	1.031	0.714
700 bps	2.897	1.620	1.033	0.716
800 bps	2.906	1.624	1.035	0.717
900 bps	2.916	1.628	1.037	0.718
1000 bps	2.926	1.632	1.039	0.719

Because $\Delta L = L_l - L_0$, Table 4 can be obtained. ΔL is obtained by combining the inductor array ($L_{Cn}, n \in N+$), which is mainly controlled by the controller and the demodulated symbol signal. Table 4 is the number table required by the look-up table method. The inductor array combination corresponding to ΔL can be determined according to the actual engineering, such as installation space, cost, etc., which will not be further elaborated in this paper.

Table 4. Inductance values $\Delta L/\mu H$ corresponding to different Baud rates and center frequencies.

| f_0 ΔL R_B	15 kHz	20 kHz	25 kHz	30 kHz
100 bps	19	7	4	3
200 bps	37	15	9	5
300 bps	57	24	13	7
400 bps	75	32	17	9
500 bps	94	40	21	12
600 bps	113	48	25	14
700 bps	133	56	29	17
800 bps	151	64	33	19
900 bps	170	72	37	21
1000 bps	189	80	41	23

4. Simulation Analysis

According to Figure 4, the simulation model can be established, and the simulation parameters are: fixed inductors $L_0 = 1.58$ mH, $L_{C1} = 10$ µH, $L_{C2} = 5$ µH, $L_{C3} = 30$ µH; the MSK signal center frequency is $f_0 = 20$ kHz; the antenna equivalent capacitance is $C_a = 39.79$ nF; the antenna equivalent radiation resistance is $R_a = 1$ Ω; and symbol rates are 200 bps, 500 bps, 1000 bps, respectively. The simulation results are as follows.

As illustrated in Figures 11a, 12a and 13a, an increase in the communication rate results in a decline of the peak voltage signal across the equivalent radiation resistance of the very low frequency antenna during traditional tuning, decreasing from approximately 40.9 V to 34.82 V. Concurrently, the fluctuations within the envelope become increasingly pronounced, with its minimum value dropping from around 38.51 V to 20.98 V. Conversely, as depicted in Figures 11b, 12b and 13b, under the SYNT-RTID synchronization control strategy, the peak voltage signal on the equivalent radiation resistance remains stable between 43.72 V and 43.93 V as communication rates rise, exhibiting both a consistent peak value and a constant envelope profile. It is evident that signals governed by the SYNT-RTID control strategy maintain significantly higher peak values compared to those observed during traditional tuning while also preserving a steady envelope.

However, as illustrated in Figures 11b, 12b and 13b, the signal experiences a period of detuning. This phenomenon arises from the fact that, according to the previously described control strategy flowchart, real-time impedance measurement necessitates a certain

duration; during this time, both the amplitude and phase of the signal do not exhibit abrupt changes when out of tune but instead undergo gradual variations. Consequently, only those impedance measurements taken after stabilization of amplitude and phase yield accurate results. At this juncture, the controller within the tuning control unit will issue corresponding enable control instructions to the logic gate unit. Upon receiving these enable instructions, the logic gate unit is primarily governed by code word sequence signals and subsequently outputs tuning control signals to the switching device. Following initial impedance measurement, which identifies necessary enabling for specific logic gates, subsequent controls are predominantly managed by code word sequence signals; thus, ensuring that at this stage, the signal remains consistently in resonance with a stable envelope.
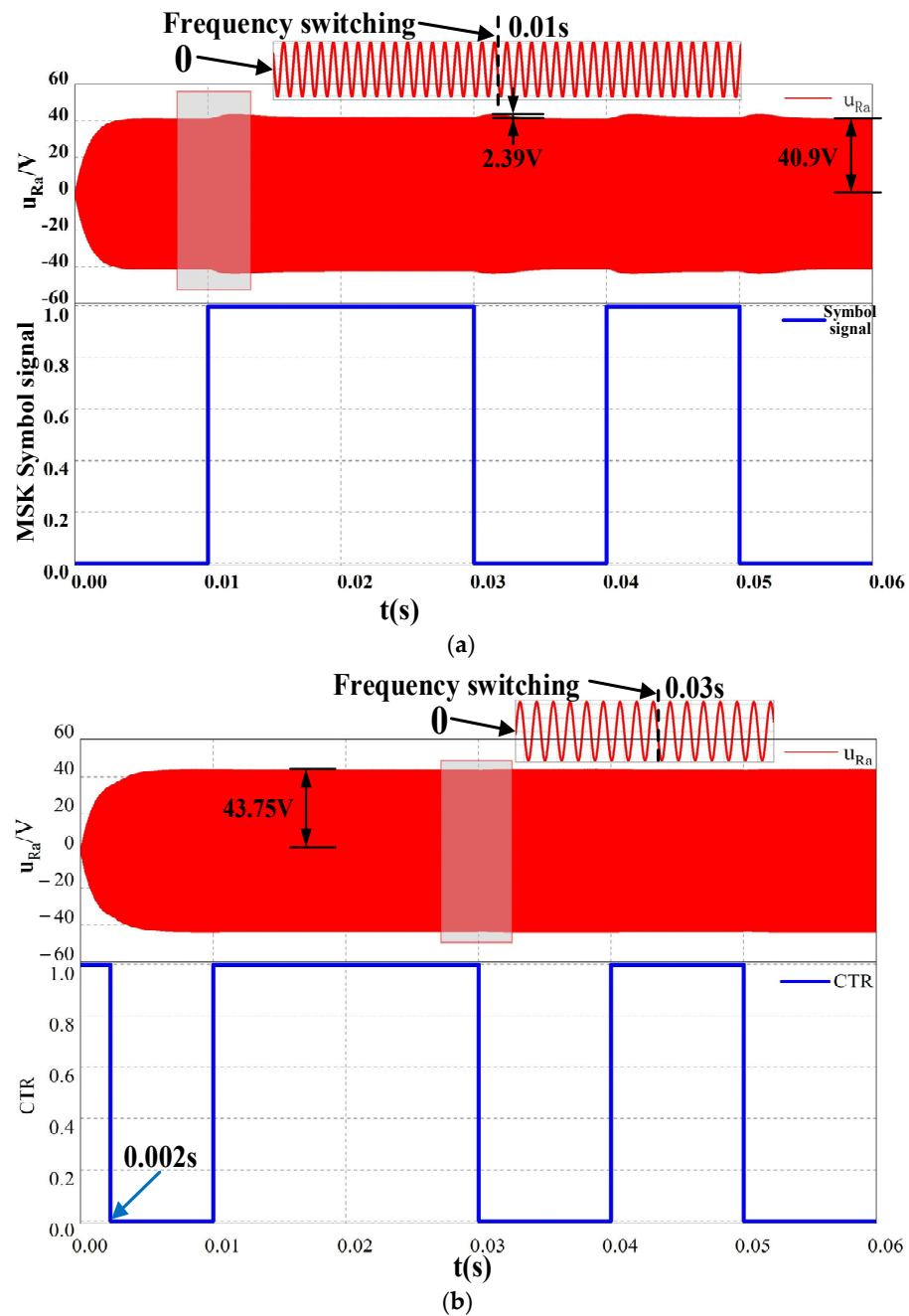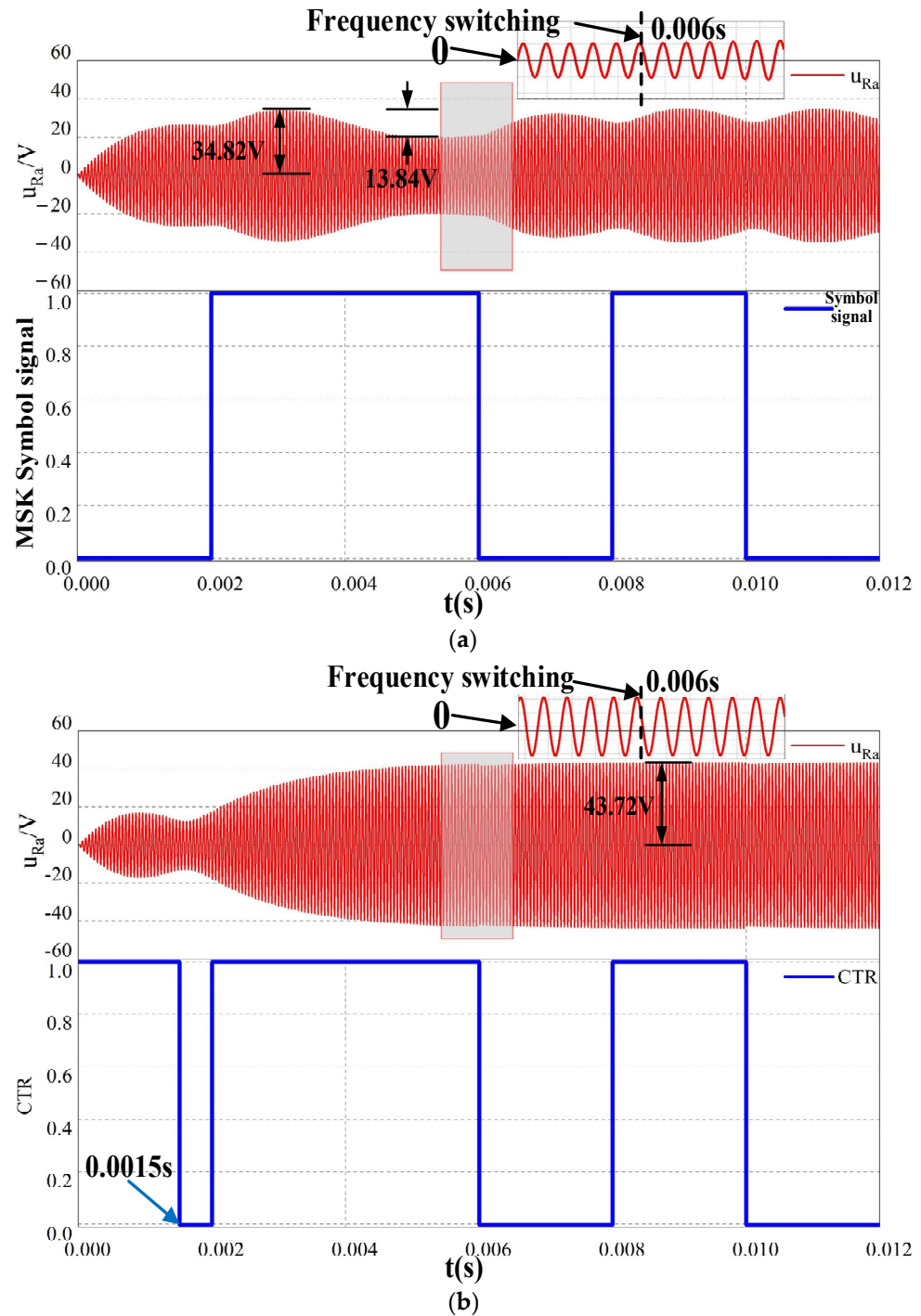
Figure 11. Time domain waveforms of the voltage signals at both ends of the R_a under different tuning modes when the communication rate is 200 bps. (**a**) Fixed tuning; (**b**) when the SYNT-RTID synchronous control strategy is used.
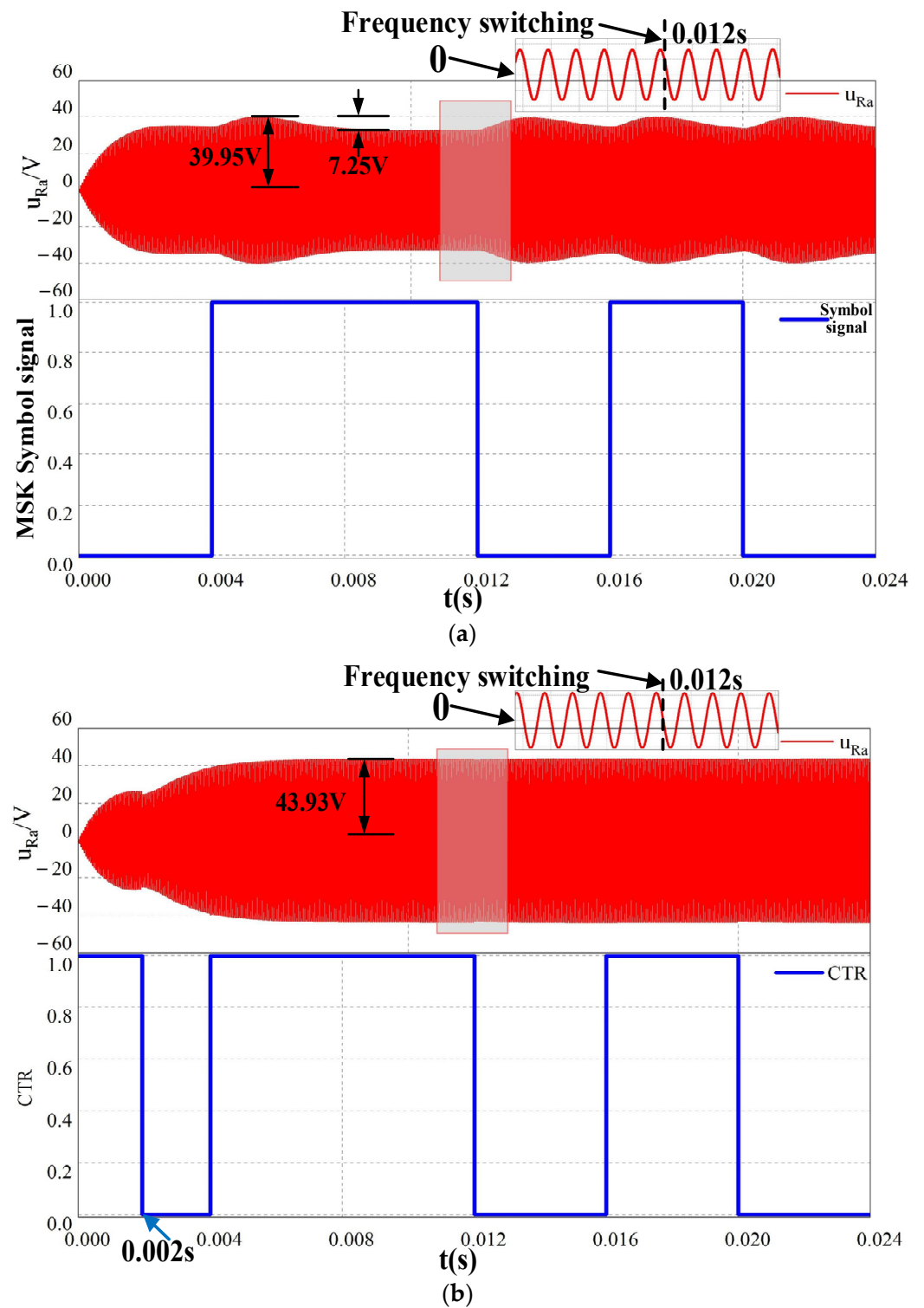
Figure 12. Time domain waveforms of the voltage signals at both ends of the R_a under different tuning modes when the communication rate is 500 bps. (**a**) Fixed tuning; (**b**) when the SYNT-RTID synchronous control strategy is used.

Figure 13. Time domain waveforms of the voltage signals at both ends of the R_a under different tuning modes when the communication rate is 1000 bps. (**a**) Fixed tuning; (**b**) when the SYNT-RTID synchronous control strategy is used.

The blue curve in Figures 11b, 12b and 13b illustrates the control signal CTR output by the tuning control unit. As depicted, the impedance measurement times are approximately 2 ms, 2 ms, and 1.5 ms, all of which are less than two code word widths; consequently, this strategy enables rapid system tuning within these constraints. During the actual message transmission process, the code word sequence is inherently random, and its overall duration extends beyond just a few milliseconds. The likelihood of encountering at least two consecutive '0' code words is significantly high; therefore, any

energy loss attributable to impedance measurement time in practical applications can be considered negligible.

5. Conclusions

This paper conducts a comprehensive analysis of inductor accuracy, establishing the appropriate precision requirements under specified conditions. Additionally, the methodology presented herein can be employed to ascertain the necessary inductor accuracy for practical applications. Furthermore, we propose a synchronous tuning control strategy for VLF communication based on real-time impedance detection, ensuring that the antenna feed system resonates with MSK signals in real time. As communication rates increase, the improvement effect of synchronous tuning on the voltage signal waveform of the equivalent radiation resistor of the VLF antenna will be more obvious. Consequently, this VLF communication synchronous tuning control system and its associated strategy can effectively expand the bandwidth of the antenna feed system and enhance communication rates within VLF transmission systems.

Author Contributions: Conceptualization, S.W.; Methodology, S.W.; Software, Y.L.; Validation, S.W.; Formal analysis, H.Z.; Resources, H.Z.; Writing—original draft, S.W.; Writing—review & editing, X.X.; Supervision, X.X.; Funding acquisition, X.X. All authors have read and agreed to the published version of the manuscript.

Institutional Review Board Statement: Not applicable.

Informed Consent Statement: Not applicable.

Data Availability Statement: The data presented in this study are available on request from the corresponding author. The data are not publicly available due to privacy.

Conflicts of Interest: The authors declare no conflict of interest.

References

1. Wen, W.F. Research on Miniaturized HF Ultra-HF Wideband Antenna and Matching Network. Master's Thesis, University of Electronic Science and Technology, Chengdu, China, 2024.
2. Dan, D. Research on Wideband and Miniaturization of Low-Frequency Antenna. Master's Thesis, University of Electronic Science and Technology, Chengdu, China, 2014.
3. Fujimoto, K.; Hirasawa, K.; Henderson, A.; Ames, J.R. *Small Antenna*; National Defense Industry Press: Beijing, China, 1991.
4. Liu, C.; Jiang, H.; Huang, J.H. *Very Low Frequency Communication*; Haichao Publishing House: Beijing, China, 2008; p. 122.
5. Sun, Y.; Yin, L.; Xiang, X. MSK engineering implementation method of digital modulation signal demodulation. *J. Comput. Appl. Softw.* **2019**, *36*, 5.
6. Fan, C.; Cao, L. *Communication Principle*; National Defense Industry Press: Beijing, China, 2006.
7. Watt, A.D. *VLF Radio Engineering*; Pergamon: Bergama, Turkey, 1967.
8. Wolff, H. High-Speed Frequency-Shift Keying of LF and VLF Radio Circuits. *IRE Trans. Commun. Syst.* **1957**, *5*, 29–42. [CrossRef]
9. Jin, G.; Dong, Y. MSK synchronization based on FPGA tuning study. *Microcomput. Inf.* **2012**, *28*, 52–53.
10. Hartley, H. Electronic Broad Banding of VLF/LF Antennas for FSK Radio Communication. *IEEE Trans. Commun. Technol.* **1971**, *19*, 555–561. [CrossRef]
11. Zhang, W.; Zheng, L.; Dong, Y. Very low frequency transmitting antenna dynamic tuning bandwidth study. *J. Ship Electr. Eng.* **2009**, *10*, 4. [CrossRef]
12. Dong, Y.; Liu, C. Dynamic tuning VLF antenna performance. *J. Nav. Eng. Univ.* **2010**, *22*, 98–102.
13. Jin, G.; Dong, Y. VLF emission system synchronous tuning study. *J. Mod. Electron. Technol.* **2011**, *34*, 3.
14. Ling, J.; Dong, Y.; Xu, H. Very low frequency transmitting system performance simulation. *J. Radio Commun. Technol.* **2015**, 74–76. [CrossRef]
15. Dong, Y.; Jiang, Y.; Zhang, J. VLF emission system based on MSK spectrum frequency characteristic study. *J. Radio Sci. J.* **2010**, *3*, 6.
16. Firman, C.M. Synchronized Turn-Off of VLF Antennae: US19720222194. U.S. Patent 3904966A, 18 June 2024.
17. Johannessen, P.R.; Planckp, V. Antenna Tuning System and Method. U.S. Patent 4689803, 1 September 1987.
18. Johnson, L.J. Magnetic Amplifier Switchfor Automatic Tuning of VIF Transmitting Antenna. U.S. Patent 5034697, 23 July 1991.
19. Ivan, W.; Ivan, W.; Guy, B. Switchable Inductor for Strong Currents and Antenna Tuning Circuit Provided with at Least One Such Inductance: FR19920005722. U.S. Patent FR2691308A1, 5 May 2024.

20. Simpson, T.; Roberts, M.; Berg, E. Developing a broadband circuit model for the Cutler VLF antenna. In Proceedings of the Antennas & Propagation Society International Symposium, Boston, MA, USA, 8–13 July 2001. [CrossRef]
21. Berg, E.C.; Roberts, M.A.; Simpson, T.L. Dual-frequency distortion predictions for the Cutler VLF array. *Aerosp. Electron. Syst. IEEE Trans.* **2003**, *39*, 1016–1034. [CrossRef]
22. Volke, A.; Hornkamp, M. *IGBT Modules: Technology, Drivers and Applications*; Infineon Technologies AG: Munich, Germany, 2012.
23. Khanna, V.K. *Insulated Gate Bipolar Transistor IGBT Theory and Design*; Wiley-IEEE Press: Hoboken, NJ, USA, 2003. [CrossRef]
24. Yan, S. (Ed.) *Foundation of Digital Electronic Technology*; Higher Education Press: Beijing, China, 2006.
25. Yang, D.; Liu, R.; Zhao, L. Three-phase high power factor rectifier current control. *J. Electrotech.* **2000**, *15*, 5.
26. Wu, X. The Improvement of Circuit Power Factor. In Proceedings of the 2nd International Conference on Material Science, Energy and Environmental Engineering (MSEEE 2018), Xi'an, China, 16–17 August 2018. [CrossRef]
27. Zu, Y.; Li, W.; Lv, Y. *Fundamentals of Circuit Analysis*, 2nd ed.; Publishing House of Electronics Industry: Beijing, China, 2014.